Materials & Design 241 (2024) 112962

Contents lists available at ScienceDirect

Materials & Design

journal homepage: www.elsevier.com/locate/matdes

Grain size prediction for stainless steel fabricated by material extrusion additive manufacturing

Siyao You [a], Dayue Jiang [b], Xiangyu Yuan [a], Fuji Wang [a], Fuda Ning [b,*]

[a] School of Mechanical Engineering, Dalian University of Technology, Dalian 116023, China
[b] Department of Systems Science and Industrial Engineering, State University of New York (SUNY) at Binghamton, Binghamton, NY 13902, USA

ARTICLE INFO

Keywords:
Additive manufacturing
Material extrusion
Sintering
Stainless steel
Grain growth
Analytical model

ABSTRACT

Most traditional powder melting-based additive manufacturing (AM) technologies generally yield high-performance parts at the expense of additional cost and energy consumption. As an economical and efficient alternative method, material extrusion (ME) that deploys polymer-based filaments with highly filled metal particles offers the possibility of scalable, low-cost fabrication of metal components. As a critical step, sintering governs the mechanical strength and geometry of the final parts. The grain growth behavior induced during sintering should be well controlled to achieve the parts with the desired mechanical performance. Due to the nature of AM, grain growth kinetics could also involve extremely complex grain boundary migration and atomic diffusion mechanisms caused by the heterogeneous pore distribution. In this work, an analytical model was developed to predict and understand the grain growth behavior of stainless steel (SS) 316L built by ME-based sintering-assisted AM. Such a model accounts for anisotropic viscosity parameters calibrated through a three-dimensional dilatometry test, enabling the prediction of grain size evolution during sintering. Grain growth kinetic parameters were further identified by the grain size data at the heating and holding stages. To validate and generalize the model, we also conducted the grain size evolution prediction under different sintering temperature profiles for as-built SS 316L specimens. This work will provide scientific insights into the grain growth behavior of metal parts built by this AM technique and its understanding can be readily transferred to other sintering-assisted AM processes like binder jetting and ink writing for metal structure creation.

Nomenclature

θ	Porosity
ρ	Relative density
$\dot{\theta}$	Porosity rate (s^{-1})
σ_{ij}	External stress tensor ($N{\cdot}m^{-2}$)
α	Surface energy ($J{\cdot}m^{-2}$)
r	Radius of powder particles (m)
φ	Shear modulus
ψ	Bulk modulus
P_L	Effective sintering stress (Pa)
δ_{ij}	Kronecker delta
$\dot{e}_{ij}$	Strain rate tensor (s^{-1})
$\dot{e}$	Trace of strain rate tensor (s^{-1})
$\dot{e}_{x,\ y,\ z}$	X, Y, and Z strain rate components (s^{-1})
η	Material viscosity (Pa·s)
$\eta_{x,\ y,\ z}$	X, Y, and Z viscosity components (Pa·s)
η_0	Viscosity pre-exponential factor (Pa·s)
T	Temperature (K)

(*continued on next column*)

(*continued*)

Nomenclature	
$\eta_{0x,\ 0y,\ 0z}$	X, Y, and Z viscosity pre-exponential factor components (Pa·s)
Q_v	Viscosity activation energy ($J{\cdot}mol^{-1}$)
G	Grain size diameter (m)
G_0	Initial grain size diameter (m)
P	Grain growth rate exponent
B	Viscosity grain size exponent
K'	Constant for isothermal condition ($m^{1+p}{\cdot}s^{-1}$)
$\dot{G}$	Grain growth rate ($m{\cdot}s^{-1}$)
K	Grain growth factor ($m^{1+p}{\cdot}s^{-1}$)
K_0	Grain growth pre-exponential factor ($m^{1+p}{\cdot}s^{-1}$)
Q_G	Grain growth activation energy ($J{\cdot}mol^{-1}$)
R	Ideal gas constant
t	Sintering time (s)

* Corresponding author.
E-mail address: fning@binghamton.edu (F. Ning).

https://doi.org/10.1016/j.matdes.2024.112962
Received 18 January 2024; Received in revised form 9 April 2024; Accepted 19 April 2024
Available online 20 April 2024

1. Introduction

Different from mainstream metal powder fusion-based additive manufacturing (AM) technologies (directed energy deposition (DED) [1], powder bed fusion (PBF) [2,3], etc.), a multi-step material extrusion (ME) metal AM approach combining printing, debinding, and sintering process is attracting the widespread attention. Specifically, wax/thermoplastic polymer-based filaments [4,5] with highly filled metal powders can be used to build the 'green' part with subsequent debinding and sintering steps required to achieve the desired finished part. This fabrication strategy shows a huge engineering application prospect in the rapid prototyping of scalable metal components with relatively low fabrication cost and limited material waste. In the past decade, ME has been developed to build a large array of metal/ceramic materials such as stainless steel (SS) (316L [5,6] and 17-4 PH [4,7]), titanium Ti-6Al-4V [8], copper [9,10], bronze [11], tungsten [12], zirconia [13], alumina [14], etc., laying a solid foundation to advance the understanding of ME processes.

As a crucial step of the ME process, sintering is a process that combines densification and coarsening or grain growth [15]. Achieving high densification with effective control of grain growth is key to improving mechanical performance and facilitating the adoption of ME for large-scale industrial applications. To obtain the desired behavior, researchers have been conducting a large number of preliminary experimental studies on the underlying mechanism of grain growth since the year of 2019 [16]. The most extensively investigated metal in literature is SS 316L [17–19]. The pioneering research of Gong et al. [20] found that the grain morphology of SS 316L fabricated by ME is different from that of metal powder fusion-based AM technologies. Thompson et al. [16] identified the ultra-large grain size of 500 μm at a heating rate of 0.2 K/min, leading to a reduction of strength by about 12 %. When the heating rate is increased to 5 K/min, the final grain structures can be stabilized at 40–50 μm with a relatively equiaxed grain morphology. Recently, applying hot isostatic pressing (HIP) [21] to the metal components after MEAM is beneficial to inhibiting grain growth, thereby producing a finer microstructure. These have advanced the fundamental understanding of the microstructure development during the sintering process in MEAM. Nevertheless, the dynamic grain growth process could not be thoroughly explained only by the ex-situ characterization of the grain size after sintering. Intermittent experiments can reproduce this invisible phenomenon. However, they require time-consuming experimental identifications at different stages of the sintering, which emphasizes the need for understanding and predicting the sintering grain growth behavior.

Early theoretical studies showed that grain growth can retard the sintering densification rate by increasing diffusion paths and sintering capillary forces, particularly at the later stage of sintering. The sintering densification process could also in turn influence the grain growth rate [22,23] through impurity segregation [13,22] or pore drag [24] in grain boundaries. Riedel et al. [25] developed a numerical model considering pores and grain boundary mobility during grain growth in porous compacts, indicating that the grain size is highly pore-dependent. Watanabe et al. [26] identified an inverse correlation between grain size and square-root fractional porosity in the traditional sintering of carbonyl iron. Manière [27,28] successfully extracted all parameters of grain growth kinetics using a simple dilatometry curve for improved densification. Olevsky [29–31] also added a function of porosity to the traditional grain growth model to simulate the grain evolution for dense materials at high temperatures. The sintering temperature profile was optimized, and the grains were highly refined using a two-step sintering method [29]. As another important factor, effects of pore size distribution on grain growth were also considered in other theoretical models developed [32–34]. For MEAM process, anisotropic sintering behavior does exist due to the heterogeneous pore distribution formed in three-dimensional printing [35]. In addition, the existing grain growth-related theories or models could be misleading and inappropriate if they are directly applied to understand and quantify the anisotropic sintering process in the specific MEAM.

The objective of this work is to predict and understand the grain size evolution during various time-dependent sintering stages of SS 316L parts built by the MEAM through a combination of analytical modeling and experiments. First, an analytical model of anisotropic sintering involving grain evolution is established based on the continuum theory of sintering and a three-dimensional dilatometry test. The relationship between grain size evolution and anisotropic viscosity is built. Then, a rapid identification method for all anisotropic sintering parameters is then developed. Based on this, experiments are employed to validate the grain growth behavior at different sintering stages. Finally, a comprehensive extraction of grain growth kinetic parameters is performed to help predict the grain size evolution of SS 316L under various sintering temperature profiles. The outcome of this work can be directly applied to the identification of sintering grain growth kinetic parameters of other pure metals/alloy materials, so as to quantify and understand the relationship between grain size evolution and sintering temperature. Such a prediction approach can also be generalized to other sintering-assisted metal/ceramic AM processes like stereolithography, binder jetting, and ink writing, thereby providing theoretical guidance for the final sintering process optimization.

2. Materials and methods

2.1. Feedstock characterization, printing, and catalytic debinding

A commercially available highly filled Ultrafuse SS 316L filament (BASF, Ludwigshafen, Germany) with a diameter of 2.85 mm can be directly used as a feedstock for extrusion printing. Printing experiments were performed on a desktop fused filament fabrication (FFF) printer (Raise 3D, Forge 1, China). Table 1 lists all the printing parameters. Three printed cube specimens had a side length of 10 mm. Then, the printed 'green' parts were conducted the catalytic debinding (1–2 mm/h for each external surface) in a thermal oven (Raise 3D, D200-E, China) at an acidic atmosphere to complete the primary binder removal (approximately 97 wt%). The residual main chain polymer as the backbone was then completely removed during the pre-sintering treatment, as detailed in the previous work of Ning et al [35].

2.2. Dilatometry test

To identify the grain growth kinetics parameter of SS 316L during the sintering process, we conducted three dilatometry tests for three equal size ($10 \times 10 \times 10\ mm^3$) pre-sintered cube specimens under a pure argon atmosphere to accurately capture the three-dimensional dynamic changes throughout the linear heating process. Specifically, three sintering tests (Linseis, DIL L75VS1600, Germany) were performed at a 5 K/min heating ramp to 1,653 K and two hours of holding for the measurements in X (In-plane), Y (In-plane), and Z (Building) directions, respectively. The defined final dilatometry testing temperature is based on the sintering profile given by DSH Technologies [36], as shown in Fig. 1. The purpose of three-directional dilatometry test is to quantify the shrinkage anisotropy. Finally, the dilatometry results of displacement and strain rate would be leveraged in the analytical modeling to

Table 1
Printing parameters for material extrusion (ME) process.

Printing parameters	Values
Nozzle temperature	230 °C
Nozzle size	0.5 mm
Infill density	100 %
Printing speed	30 mm/s
Layer thickness	0.2 mm
Bed temperature	100 °C
Filament preheating temperature	60 °C

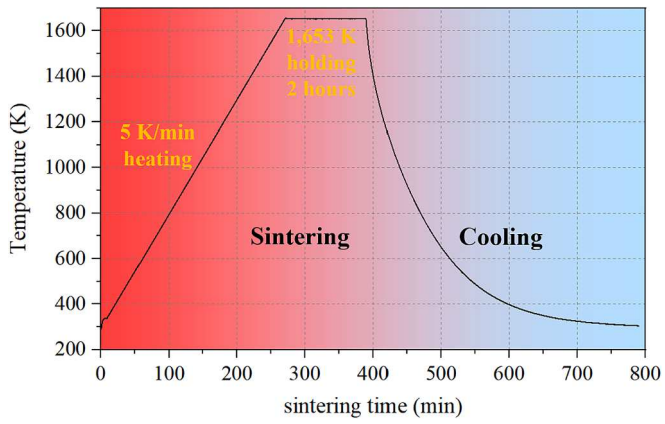

Fig. 1. Sintering temperature profile for dilatometry test.

achieve the prediction of grain size evolution.

2.3. Thermal debinding and sintering experimental design

To remove the residual main chain polymers (approximately 3 wt%) from the 'brown' parts, the thermal debinding process was performed in a tubular furnace (SK-G08163-3-600) under a pure argon atmosphere. The temperature setting details can refer to the previous work of Ning et al. [35]. Then, we adopted an intermittent linear heating. Specifically, eight groups of sintering experiments were carried out: (1) Heating to 1,503 K, 1,533 K, 1,563 K, 1,593 K, 1,623 K, and 1,653 K at a rate of 5 K/min with a dwell time of 5 min for each temperature, and then cooling from each one above to the room temperature; (2) Sintering with a holding time of 60 min and 120 min, respectively, at 1,653 K. Each set of sintering parameters was repeated five times for the fabrication to ensure the experimental repeatability. Based on previous studies [37], the sintering temperature interval was set to 30 K to characterize the grain size evolution during sintering process in MEAM. Fig. 2 displayed the intermittent sintering experimental design employed in this study.

2.4. Microstructure observation

The element content of SS 316L cube specimen after dilatometry test were analyzed by inductively coupled plasma optical emission spectrometry (ICP-OES) (Agilent 5800, Agilent Technologies) and high-frequency infrared carbon and sulfur (CS) analyzer (Corey-200, Deyang Kerui Instrument, China). The section morphology of BASF Ultrafuse filament and the microstructure of SS 316L specimen were characterized by a scanning electron microscope (SEM, Nova NanoSEM 450, FEI Corp., USA) equipped with electron backscattered diffraction (EBSD) analyzer. The microstructure and grain orientation of SS 316L specimen (after dilatometry test) after mechanical grinding and electropolishing were conducted with an acceleration voltage of 30 keV and a step size of 1 μm. EBSD data processing was conducted using TSL OIM analysis 7. Mechanically ground, polished, washing, and electrolysis were performed on the sintered specimens at various temperatures to highlight the grain structures. The microstructural evolution of SS 316L specimens sintered at various temperatures were characterized by optical microscopy (Olympus Corporation, BX53M, Tokyo, Japan). And the images were captured in five different regions of the same cube. The Image analysis was carried out on ImageJ software and the grain size data was measured based on the intercept method. The measurement of grain size follows the standard method of ASTM E1382-97. The weight and dimensions of pre-sintered 'brown' parts were measured, and the initial relative density can be calculated by dividing the density of the pre-sintered specimen to the dense SS 316L (7.98 g/cm^3).

3. Analytical modeling for grain size prediction

The model developed in this work involves the unique three-directional anisotropic shrinkage characteristics of the pre-sintered specimens. The sintering model is a continuum-mechanics (CM) one developed based on the theories of plastic and nonlinear-viscous deformation of porous bodies [22]. A porous body is defined as a two-phase material including the skeleton and pores. It is assumed that the particles are perfect spheres, and the viscous behavior is linear in all directions. This approach covers theoretical relations among the sintering stress, compaction moduli, and temperature-dependent properties of material viscosity, which is widely applied to uncover the sintering behavior of ceramic/metal 'brown' parts. The stress–strain relationship to describe the densification of a continuous compressible medium is defined as [22,31]:

$$\sigma_{ij} = 2\eta\left(\varphi\dot{e}_{ij} + \left(\psi - \frac{1}{3}\varphi\right)\dot{e}\delta_{ij}\right) + P_L\delta_{ij} \tag{1}$$

where σ_{ij} corresponds to external stress tensor, η is the material viscosity of a fully dense material, $\dot{e}_{ij}$ is strain rate tensor, $\dot{e}$ is the trace of strain rate tensor, showing the rate of the volume evolution in a porous body, δ_{ij} is Kronecker delta, φ is shear modulus, ψ is bulk modulus, and P_L is effective sintering stress.

In a Cartesian coordinate system, the porosity evolution can be determined locally through the following mass conservation equation:

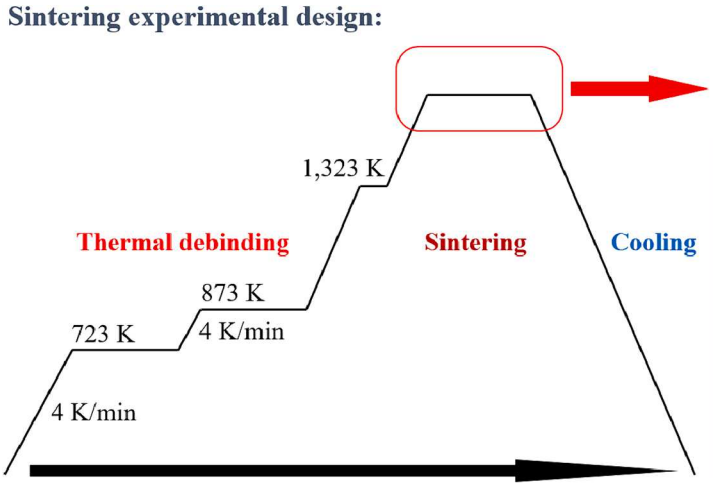

Experimental number	Sintering temperature	Heating rate	Dwell time
1	1,503 K	5 K/min	5 min
2	1,533 K	5 K/min	5 min
3	1,563 K	5 K/min	5 min
4	1,593 K	5 K/min	5 min
5	1,623 K	5 K/min	5 min
6	1,653 K	5 K/min	5 min
7	1,653 K	5 K/min	60 min
8	1,653 K	5 K/min	120 min

Fig. 2. Intermittent sintering experimental design.

$$\frac{\dot{\theta}}{1-\theta} = \dot{e}_x + \dot{e}_y + \dot{e}_z \tag{2}$$

where θ is porosity, $\dot{\theta}$ is porosity rate. Shear modulus φ, bulk modulus ψ, and effective sintering stress P_L can all be theoretically approximated as the function of porosity θ, as:

$$\varphi = (1-\theta)^2 \tag{3}$$

$$\psi = \frac{2(1-\theta)^3}{3\theta} \tag{4}$$

$$P_L = \frac{3\alpha}{r}(1-\theta)^2 \tag{5}$$

where r is the radius of powder particles, and α is surface energy. Considering the anisotropic sintering shrinkage behavior of the pre-sintered 'brown' part along X (In-plane), Y (In-plane), and Z (Building) directions, the analytic equation describing the sintering densification is obtained (see Appendix A for detailed derivation):

$$\dot{\theta} = \frac{-P_L(1-\theta)}{6\psi}\left(\frac{1}{\eta_x}+\frac{1}{\eta_y}+\frac{1}{\eta_z}\right) \tag{6}$$

In the later stage of the sintering process, grain growth is observed. The grain size dependence of material viscosity can be defined by [27]:

$$2\eta = \eta_0\left(\frac{G}{G_0}\right)^b T\exp\left(\frac{Q_v}{RT}\right) \tag{7}$$

where b is viscosity grain size exponent, η_0 is viscosity pre-exponential factor, G is grain diameter, G_0 is initial grain diameter, R is ideal gas constant, Q_v is viscosity activation energy, and T is temperature. Substituting the expression of the sintering stress P_L and the viscosity η in Eq. (6), the temperature dependence of grain size can be defined by isolating the grain size item again:

$$\frac{G^{b+1}}{G_0^b} = \frac{-2(1-\theta)^3}{\dot{\theta}T\psi}\left(\frac{\alpha}{\eta_{0x}\exp\left(\frac{Q_{vx}}{RT}\right)}+\frac{\alpha}{\eta_{0y}\exp\left(\frac{Q_{vy}}{RT}\right)}+\frac{\alpha}{\eta_{0z}\exp\left(\frac{Q_{vz}}{RT}\right)}\right)(b=3) \tag{8}$$

The equation above indicated that uniaxial viscosity could not accurately characterize grain growth during the ME process.

4. Quantification of grain growth parameters

In this section, we will uncover the sintering grain size evolution in MEAM based on the dilatometry test data. The experimental three-directional shrinkage results of cube specimens obtained through dilatometry tests are given in Fig. 3(a). Earlier sintering data (below 773 K) is removed to exclude the effect of early sintering size fluctuation caused by thermal expansion/softening. As expected, the final linear shrinkages and dilatometry conclusions of the sintered specimens displayed a satisfactory agreement: the pre-sintered specimens exhibited obvious anisotropic shrinkage behavior during the sintering (17.36 %, 18.05 %, and 20.03 % along X (In-plane), Y (In-plane), and Z (Building) directions, respectively). Based on the dilatometry experimental data, we can identify θ, $\dot{e}_x$, $\dot{e}_y$, and $\dot{e}_z$. The corresponding parameters φ and ψ can be further determined by porosity θ. The particle size of the powder particles in filament is about 6 μm [38]. It has been reported that SS 316L has no obvious grain growth behavior below 1,473 K [39]. A certain amount of sintering necks has been formed among SS 316L particles. The sintering process can be divided into two stages, corresponding to different grain size evolution behaviors: (1) almost no grain growth for temperatures below 1,473 K; (2) grain growth from 1,473 K to 1,653 K holding stage.

Thus, the material viscosity η remains the only one unknown parameter. For solid-state sintering, viscosity is related to grain boundary thickness, atomic volume, diffusion coefficient, and other parameters. This need to be calibrated with the help of a large number of mechanical property testing experiments. It is necessary to find an

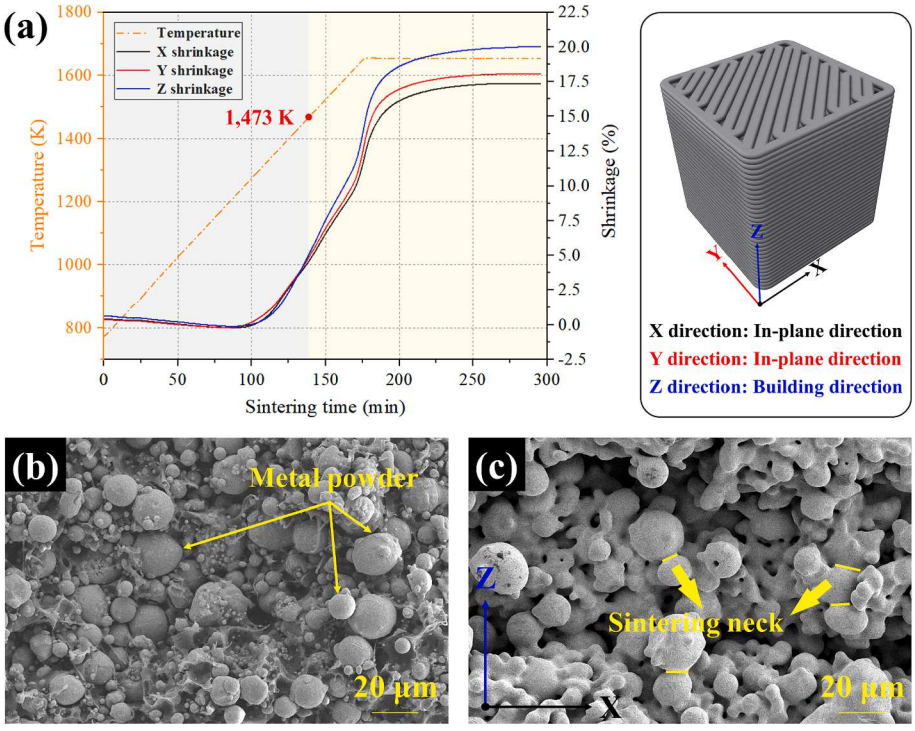

Fig. 3. (a) Dilatometry results of cube specimens, cross-section SEM images of (b) Ultrafuse SS 316L filament (SS 316L particles are wrapped by polyformaldehyde-based binder system) and (c) SS 316L cube specimen sintered at 1,473 K.

innovative method for a rapid identification and quantification of viscosity parameters. A flowchart is provided to summarize the overall modeling procedure, as illustrated in Fig. 4. The anisotropic viscosity parameters at constant grain state can be determined by combining the sintering continuum-mechanics model with dilatometry data, and the grain size term can be separated to conduct the evolution process prediction. Section 4.1 will elucidate the determination of anisotropic viscosity parameters during the early sintering stage (below 1,473 K) through a multi-step regression approach.

4.1. Sintering below 1,473 K

The anisotropic viscosity in Eq. (22) (see Appendix A) can be expressed by Eq. (9). The derivation steps in X (In-plane) direction are selected for an illustration.

$$\eta_x = \frac{-P_L}{2\left(\left(\psi+\frac{2}{3}\varphi\right)\dot{e}_x+\left(\psi-\frac{\varphi}{3}\right)\dot{e}_y+\left(\psi-\frac{\varphi}{3}\right)\dot{e}_z\right)} \tag{9}$$

Here, for another unknown (surface energy α) in the expression of sintering stress P_L, we can circumvent this problem by extracting and eliminating surface energy using the following regression equation [40]:

$$ln\left(\frac{-6(1-\theta)^2G_0^b}{G^{b+1}\left(\left(\psi+\frac{2}{3}\varphi\right)\dot{e}_x+\left(\psi-\frac{\varphi}{3}\right)\dot{e}_y+\left(\psi-\frac{\varphi}{3}\right)\dot{e}_z\right)T}\right)=ln\left(\frac{\eta_{0x}}{\alpha}\right)+\frac{Q_{vx}}{RT} \tag{10}$$

According to SEM results in Fig. 3, we can assume that the initial grain size G_0 is approximately equal to the powder particle size ($G = 2r \approx 6$ μm). Therefore, the important purpose of this stage is to determine the densification parameters with a constant particle size. The density of the pre-sintered 'brown' part is measured to be 3.91 g/cm^3, representing the initial relative density of the pre-sintered cube specimen is set to 0.49.

Using the densification data (θ, $\dot{e}_x$, $\dot{e}_y$, $\dot{e}_z$) from dilatometry tests and a linear regression fitting of Eq. (10), the anisotropic viscosity activation energies are obtained as $Q_{vx} = 205.8$ KJ·mol^{-1}, $Q_{vy} = 196.46$ KJ·mol^{-1}, and $Q_{vz} = 193.9$ KJ·mol^{-1}, respectively (see Fig. 5), indicating a mean value of 198.72 KJ·mol^{-1}. For sintering process in MEAM, the anisotropic viscosity activation energy results along three directions indicate that the thermal activation mechanism could be anisotropy. For porous bodies with heterogeneous pore distribution, lower viscosity along one direction can be explained by lower deformation resistance [41] caused by looser powder particle packing mode along that direction (e.g., interlayer pores along Z building direction).

The pre-exponential viscosity factor ratios exhibited anisotropic responses during the curve fitting process. This numerical difference in three directions cannot be considered as a constant value in isotropic materials. The pre-exponential factor could be dependent on porosity.

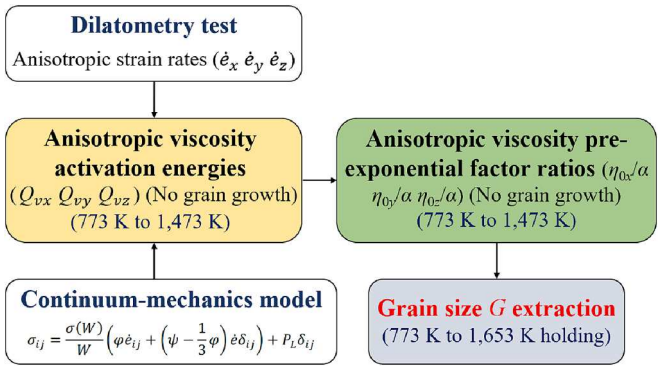

Fig. 4. The main procedures of the sintering model.

To quantify the formation and attenuation of the anisotropy, the pre-exponential factor ratio in Eq. (10) was re-extracted in Eq. (11) below to predict the connection between the pore evolution and anisotropic behavior. The porosity dependence of the three-directional pre-exponential factor ratios (η_{0x}/α, η_{0y}/α, and η_{0z}/α) are shown in Fig. 6.

$$\frac{\eta_{0x}}{\alpha}=\frac{-6(1-\theta)^2G_0^b}{G^{b+1}\left(\left(\psi+\frac{2}{3}\varphi\right)\dot{e}_x+\left(\psi-\frac{\varphi}{3}\right)\dot{e}_y+\left(\psi-\frac{\varphi}{3}\right)\dot{e}_z\right)Texp\left(\frac{Q_{vx}}{RT}\right)} \tag{11}$$

4.2. Sintering from 1,473 K to 1,653 K holding

Using the anisotropic viscous parameters shown in Fig. 6, we can initially obtain the grain size evolution curve from 1,473 K to 1,653 K in Fig. 7 (isolate G of Eq. (8)). During the initial sintering stage, almost no grain growth occurs until 1,473 K where it becomes active. The reason can be explained by sintering neck formation during the initial stage of sintering (intergranular through nucleation, crystallization). On the other hand, weaker mass transport at low temperature stage could not drive grain boundary migration.

5. Experimental validation and discussion

For MEAM process, residual carbon (C) caused by unremoved binders after debinding could seriously contaminate and harden stainless steel components, potentially affecting subsequent grain size characterization and analysis. The C content assessment is thus essential. In order to ensure low C characteristics, C content in SS with high plasticity and corrosion resistance is usually less than 0.03 wt% [42]. As displayed in Table 2, the chemical composition of SS 316L cube specimen after dilatometry test is characterized by ICP and CS analysis. After two steps of debinding, the C content in the system decreased from 2.434 wt% in filament to 0.023 wt% after dilatometry test. This indicates that the specimen was not contaminated by C.

The microstructures of SS 316L cube specimen after dilatometry test along Z (building) direction are characterized in Fig. 8. For MEAM process, layer-by-layer deposition during printing step can form a large number of interlayer pores in 'brown' parts, which could also be reflected in the final metal parts (see Fig. 8(a) and (b)). Such interlayer structures are discussed in detail in the previous work of Ning et al. [35]. EBSD result (see Fig. 8(c)) indicates that the cube specimen exhibit equiaxed austenite grains with a large number of annealing twinning structures. Even with the presence of interlayer gaps left over from the printing step, the grain orientation is highly random. The average grain size of cube specimen after dilatometry test is 43.9 μm (see Fig. 8(d)), which is almost exactly consistent with the modeling result of 42.6 μm. The size error is less than 2 %. Therefore, the average initial particle size of 6 μm used to determine the viscosity parameter is reasonable.

To further verify the modeling results, the statistical results of average grain size and microstructures under eight selected temperature nodes are shown in Fig. 9 for a comprehensive model validation. Combined with the analysis of EBSD results (43.9 μm) in Fig. 8, it is found that the average grain size increases from 9.95 μm at 1,503 K to 40.39 μm at 1,653 K holding 120 min. In addition, the grain grows rapidly during the 1,653 K holding stage, almost exactly representing the result and trend in Fig. 7. The difference between experimental and modeling results is approximately 5.6 %, indicating the high accuracy of our modeling and quantification methods. Approximations/assumptions during analytical modeling could lead to deviations between experimental and theoretical results.

In comparison to parts fabricated by metal injection molding or other sintering processes, larger interlayer pores are the unique structures existed in the MEAM process, causing three-directional anisotropic pore distribution, thus resulting in anisotropic shrinkage during sintering at the macroscopic level. For those sintered parts, such pores are not isolated spheres but are inter-connected. Earlier studies have demonstrated

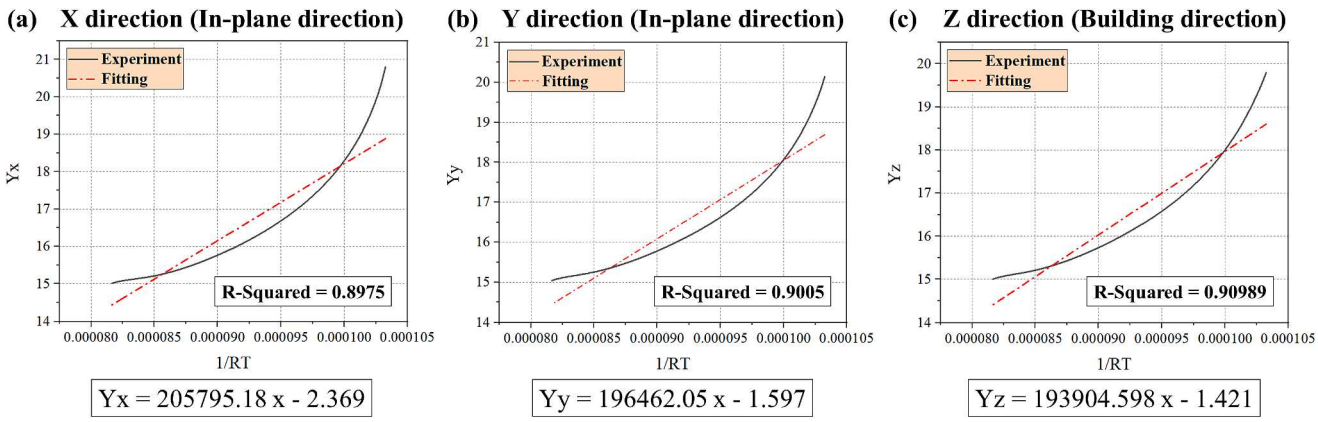

Fig. 5. Extraction of viscosity activation energies using regression analysis.

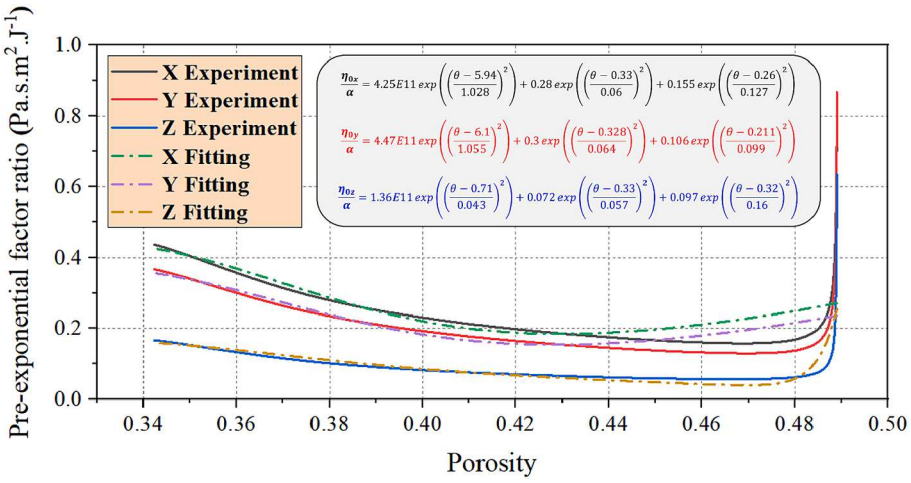

Fig. 6. Extraction of viscous pre-exponential factor ratios and corresponding fitting equations.

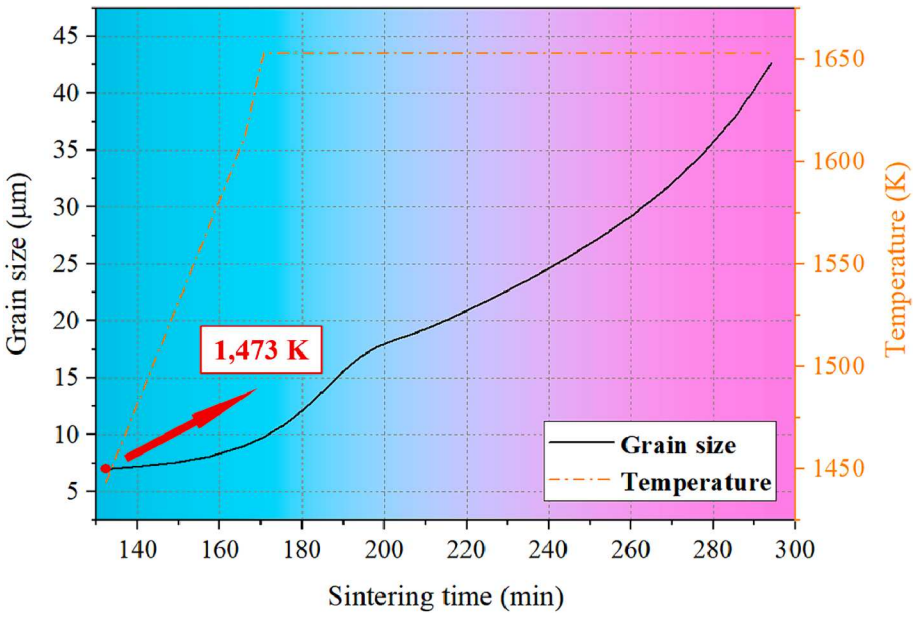

Fig. 7. Modeling results of grain size evolution with 5 K/min heating and 1,653 K holding.

Table 2
Chemical elements of SS 316L cube specimen after dilatometry test (wt.%).

Fe	Ni	Cr	C	Mo	Mn	Si	Cu	Co
Bal.	12.362	18.252	0.023	1.985	1.082	0.453	0.250	0.107

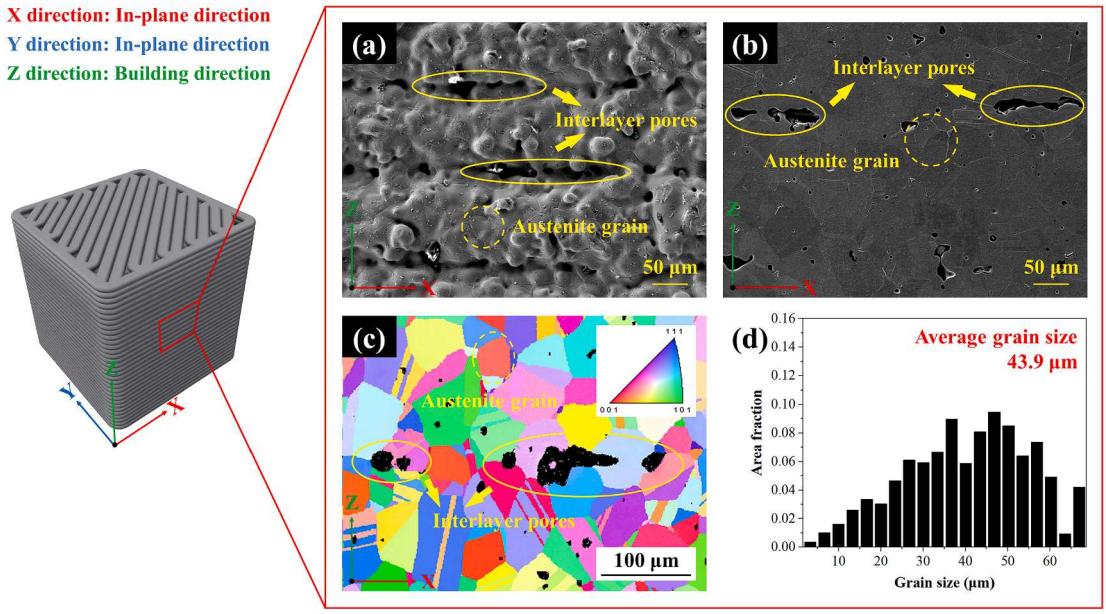

Fig. 8. (a) Interlayer microstructure, (b) Grain morphology, (c) Grain orientation, and (d) Average grain size distribution of SS 316L cube specimen after dilatometry test.

that the applied continuous thermal cycle provides free energy required for atomic diffusion to drive the grain boundary motion between grains and pores [43,44]. Another significant role of continuous thermal cycle is to bypass obstacles [45] such as impurities (solute resistance), second phase particles, or pores. When the free energy barrier caused by this hindrance is sufficiently to suppress grain boundary migration driving, grain growth is retarded or terminated [46]. Therefore, the connected interlayer pores will be a significant obstacle that interferes with grain growth. Such inherent large interlayer pores exist throughout the sintering process. In conclusion, the grain growth is impeded near the interlayer pores by the high value of porosity along *Z* (building) direction. The large pores caused by the interlayer defects after printing will slow down the grain boundary mobility, and then result in a lower grain size level on both sides of the interlayer lines. The model can only predict the evolution of average grain size. For such unique microstructure of ME-fabricated components, further accurate prediction of local grain size is required.

Finally, to verify the reliability of the grain size prediction method, the porosity of SS 316L 'brown' part during ME process can be quantified by the identified parameters G, Q_v, η_{0x}/α, η_{0y}/α, and η_{0z}/α. The comparison of porosity obtained between mass conservation equation (see Eq. (2)) and modeling (see Eq. (8)) is shown in Fig. 10, indicating the accuracy of the grain size evolution behavior predicted by the new sintering model at both initial heating stage and final holding stage. In addition, the entire modeling method can be applied to conduct the grain size prediction of various metal materials during solid-phase sintering process.

6. Model generalization

The grain size prediction model can be generalized by further identifying grain growth kinetic parameters to calculate and quantify the grain size evolution at different sintering temperature profiles. It can be seen from Fig. 7 that the grain growth rate is significantly accelerated above 1,473 K, which can be utilized to fit the traditional grain growth model, described by [46]:

$$G^{p+1} = G_0^{p+1} + K't \text{ For isothermal conditions} \tag{12-1}$$

$$G^{p+1} = G_0^{p+1} + K(T)t \text{ For anisothermal conditions} \tag{12-2}$$

where G is grain diameter, p is grain growth rate exponent ($p+1$ between 2 and 4) that corresponds to various grain growth mechanisms (4 for surface diffusion-controlled grain growth mechanism, 3 for lattice diffusion-controlled grain growth mechanism, and 2 for boundary-controlled grain growth mechanism in pure or doped system [22,24,47]). During the isothermal sintering process for fully dense or porous materials, K' is often expressed as a constant. For anisothermal conditions, the temperature effect on K needs to be reconsidered. The traditional grain growth rate is usually modeled by the following equation:

$$\dot{G} = \frac{K(T)}{G^p} \tag{13}$$

$$K(T) = K_0 \exp\left(\frac{-Q_G}{RT}\right) \tag{14}$$

where K_0 is grain growth Arrhenius pre-exponential constant, Q_G is grain growth activation energy. However, we still have another two unknown parameters, K_0 and p. All of them are of high importance for the grain growth analytical modeling to quantify the grain growth kinetics.

Based on modeling results under 1,653 K holding stage (see Fig. 7), the grain growth rate exponent p can be estimated. Eq. (15) presents the logarithm form of Eq. (14). It can be determined in the form of a linear regression of the logarithm of the grain size G and the grain growth rate $\dot{G}$. However, $\dot{G}$ is unknown, and we can perform least square fitting on

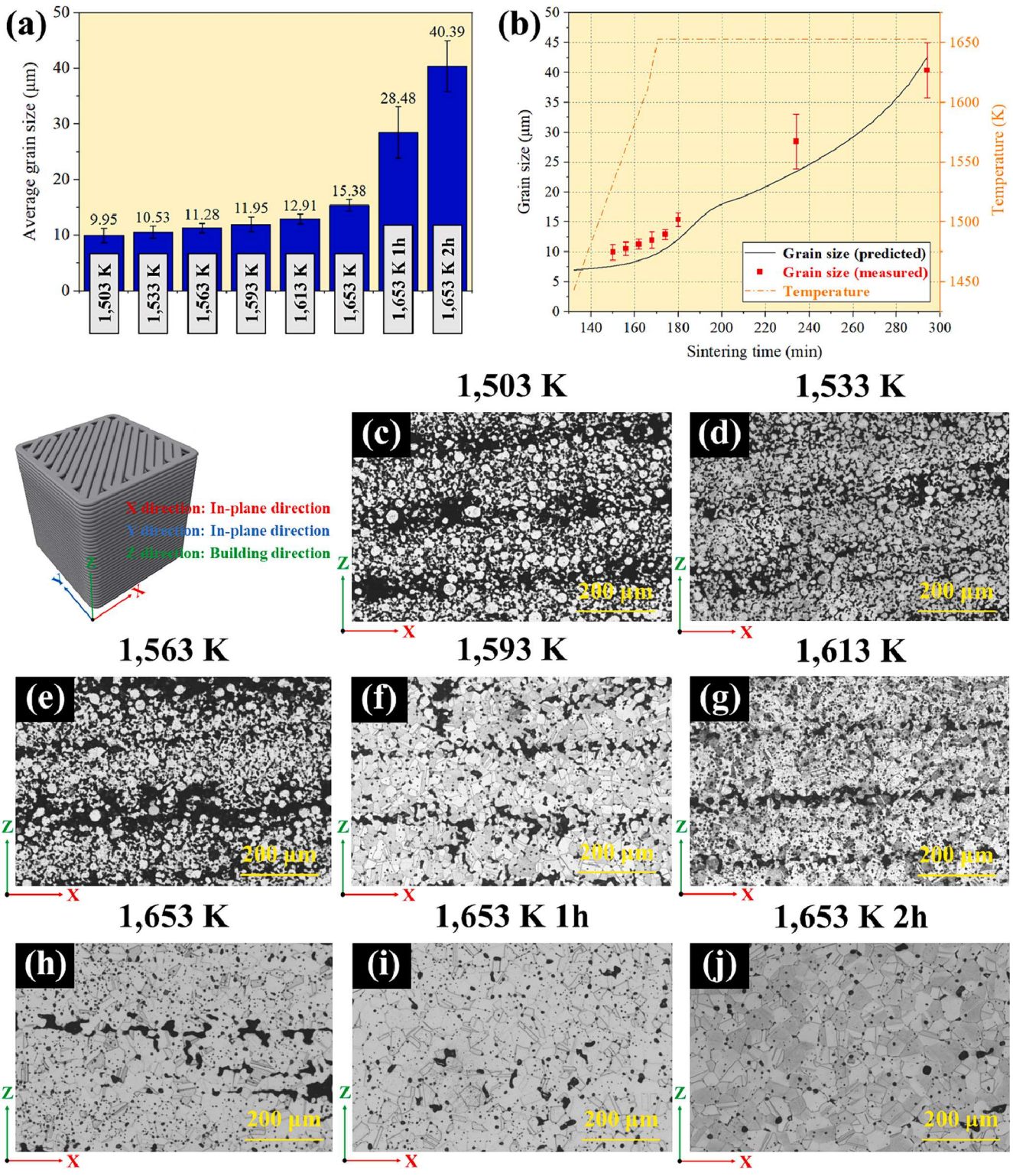

Fig. 9. (a) Average grain size statistics, (b) Comparison between modeling results and experimental data, (c)-(j) Optical micrographs showing the same area of eight cube specimens.

the collected grain size data for obtaining the grain growth rate curve. In order to obtain a more accurate $\dot{G}$ value, segment fitting is performed with the slope mutation of the curve in Fig. 7 as segmentation. The fitting mathematical equations can be expressed as the following exponential forms:

$$ln\left(\dot{G}\right) = -pln(G) + \left(ln(K_0) - \frac{Q_G}{RT}\right) \tag{15}$$

$$G_{fit1} = 5.92\text{E}-06\exp(-6.43\text{E}-06t) + 1.16\text{E}-08\exp(5.9\text{E}-04t) \tag{16}$$

$$G_{fit2} = 3.87\text{E}-06\exp(1.27\text{E}-04t) + 3.25\text{E}-12\exp(8.17\text{E}-04t) \tag{17}$$

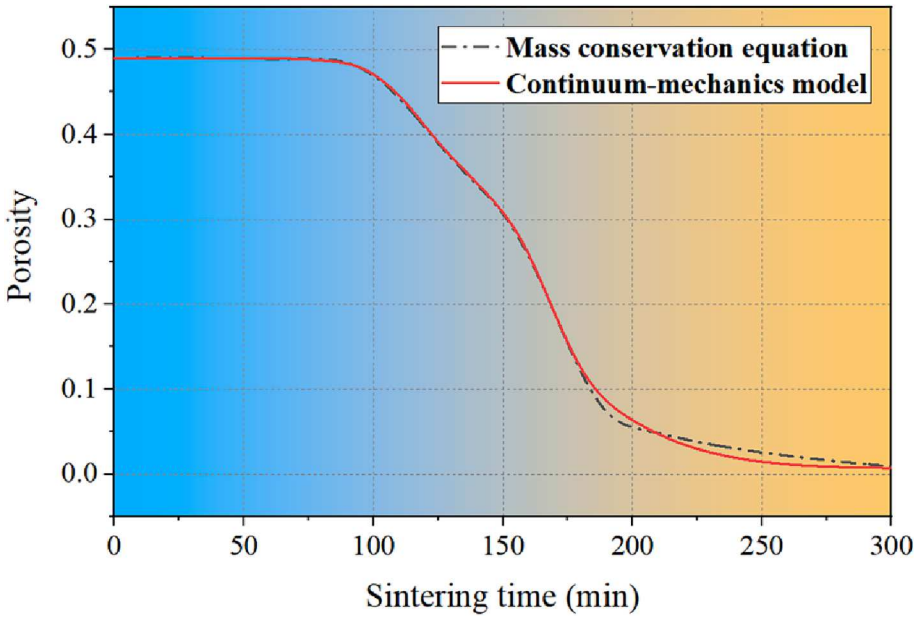

Fig. 10. Comparison between mass conservation equation and modeling predicted results.

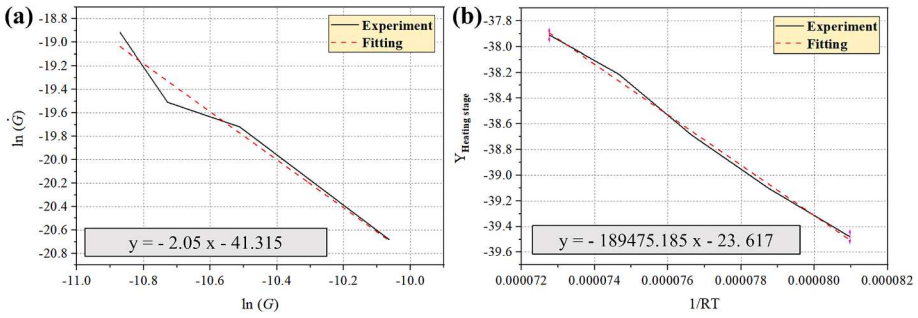

Fig. 11. (a) Linear regression for the identification of grain growth rate exponent p, (b) Determination of grain growth kinetic parameters (Q_G and $K_{0,\ \text{heating}}$).

And then, we obtained the p value of 2.05 and K_{holding} (T) value of 1.14E-18 $m^{1+p}.s^{-1}$ (see Fig. 11(a)), considering the evolution of grain growth mechanism (consistent with the boundary-controlled grain boundary migration mechanism during the later stage of sintering ($p = 2$) [22,24]) based on the results of German et al. [43].

According to the above modeling parameters and assumes the dominant densification mechanism of grain boundary diffusion ($b = 3$), the two-stage grain growth kinetic behaviors can be directly predicted. Specifically, as described in Eq (18), the grain growth activation energy can also be obtained in the form of linear regression. The fitting result is given in Fig. 11(b). We obtained the following grain growth kinetic parameters: Q_G = 189.475 KJ·mol^{-1}, $K_{0,\ \text{heating}}$ = 5.536E-11 $m^{1+p}.s^{-1}$ from 1,473 K to 1,653 K. Using the Q_G and the grain size data of 1,653 K holding stage, we can calibrate the $K_{0,\ \text{holding}}$ value of 1.108E-12 $m^{1+p}.s^{-1}$.

$$ln\left(\dot{G}G^{p}\right) = ln(K_0) - \frac{Q_G}{RT} \tag{18}$$

In order to further broaden the model application range, 1,673 K, 1,633 K, 1,613 K, and 1,573 K are selected as sintering temperatures with a 5 K/min heating ramp and a two-hours holding time, respectively, to predict the grain size evolution during the sintering process in ME. As reported in Fig. 12, the grain size of SS 316L at various sintering temperatures changed significantly during the holding stage. When the sintering temperature reaches 1,673 K, the final grain size of SS 316L is greater than 50 μm, indicating high sensitivity of grain size to temperature at higher sintering temperatures. It is also found that the final grain size of the specimen at 1,633 K is almost the same as that at 1,653 K in Fig. 7. In summary, the maximum error of final grain size is less than 10 %, indicating a good accuracy of the kinetic parameters and the applicability of the modeling method.

7. Outlook: Solute element segregation and grain growth inhibition

Solute resistance (the resistance to grain boundary migration caused by solute element segregation) can effectively inhibit the grain growth [48], limiting the grain boundary mobility. This phenomenon can be explained by the solute drag theory [49]. Excessive Cr precipitation ($Cr_{23}C_6$) at grain boundaries could also lead to a reduction in elongation and cause material embrittlement [16], thereby minimizing their potential applications. Based on the previous work of Ning et al. [50], the mechanism of Cr segregation and aggregation at the grain boundaries during the final holding stage of sintering process was revealed. Cr_3C_2 has been reported as an effective grain growth inhibitor for the consolidation of WC-Co alloys [51]. Therefore, we can further combine solute resistance with interlayer pore resistance to fully explore the grain growth mechanism. The sintering temperature profile will be optimized by controlling the grain boundary segregation rate of the solute elements, providing a new way for the grain growth inhibition during the sintering process in ME.

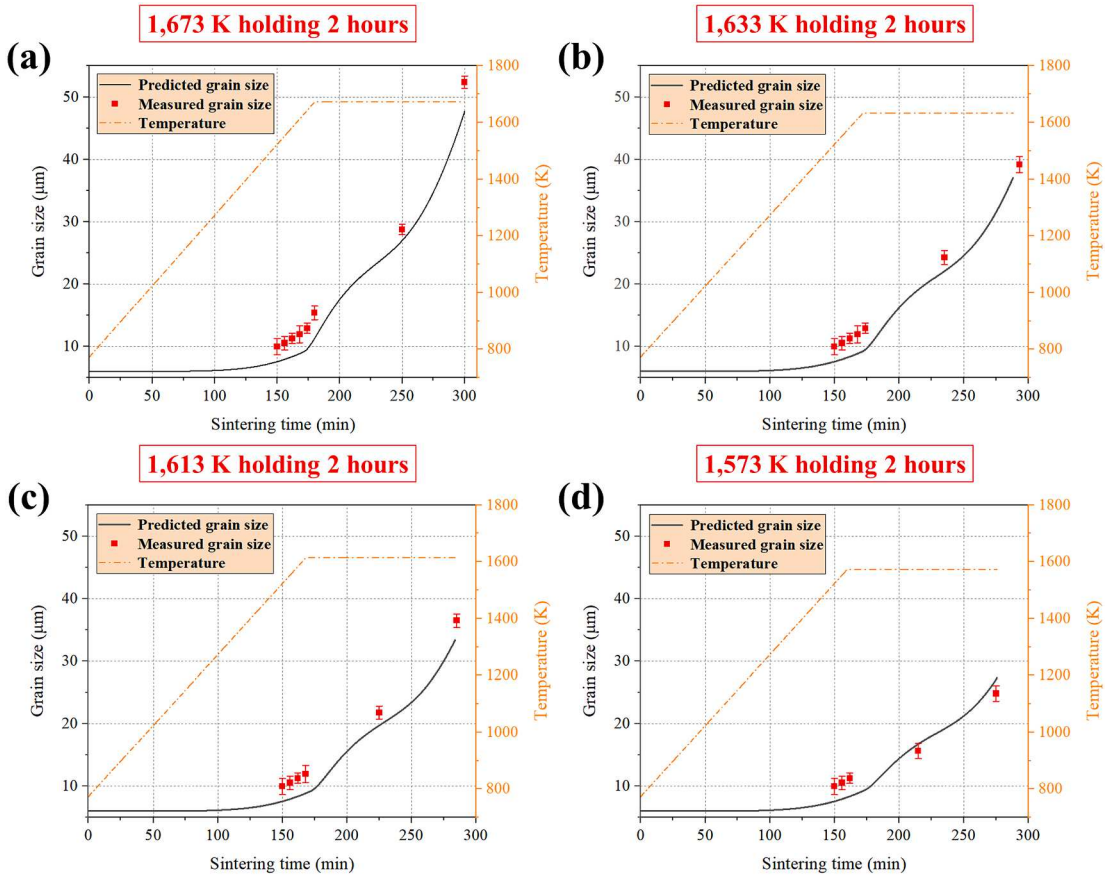

Fig. 12. Grain size evolution curve under different sintering temperature profiles: (a) 1,673 K holding 2 h, (b) 1,633 K holding 2 h, (c) 1,613 K holding 2 h, (d) 1,573 K holding 2 h.

8. Conclusions

In this work, the sintering grain growth behavior during the ME process of SS 316L was studied. A grain size prediction model involving anisotropic sintering process in ME was established for the first time. Based on this, a comprehensive prediction of grain size evolution under different sintering temperature profiles in ME was further achieved. The core research findings in this work are summarized as follows:

(1) The anisotropic sintering analytic model indicated that anisotropic viscosity could be a non-negligible factor affecting grain growth during the ME process. By combining the analytical model with the dilatometry data below 1,473 K, anisotropic response and porous dependence of the pre-exponential factor were identified.
(2) The intermittent sintering experiment results confirmed the consistency and accuracy of the analytical modeling method with acceptable errors of 5.6 %. In addition, the interlayer microstructure after sintering revealed that the macro-pore pinning caused by the magnified interlayer defects after printing can slow down the grain boundary mobility.
(3) The identification of grain growth kinetics parameters was conducted using the predicted grain size data. Compared with the data from literature, fitting results indicated a grain growth activation energy of 189.475 KJ·mol^{-1} and a grain growth rate exponent of 2, representing boundary-controlled grain growth mechanism.
(4) Based on the determined parameters of grain growth kinetics, the grain size evolution prediction was enabled at four sintering temperature profiles (1,673 K holding 2 h, 1,633 K holding 2 h, 1,613 K holding 2 h, and 1,573 K holding 2 h). The maximum error of final grain size between predicted and measured was less than 10 %. Finally, considering the Cr grain boundary segregation effect on grain boundary migration, the sintering grain growth inhibition for the solute segregation rate control was determined.

The sintering modeling method used in this work can be applied in finite element codes to predict the deformation behaviors of complex structures built by the ME process. The grain size prediction method can also be used to formulate the optimal sintering heating process of other metal alloy/ceramic materials in ME, thus avoiding a large number of trial-and-error experiments.

CRediT authorship contribution statement

Siyao You: Writing – review & editing, Writing – original draft, Visualization, Software, Methodology, Data curation, Conceptualization. **Dayue Jiang:** Writing – review & editing, Validation, Methodology, Investigation, Conceptualization. **Xiangyu Yuan:** Methodology, Data curation. **Fuji Wang:** Supervision, Resources, Funding acquisition. **Fuda Ning:** Writing – review & editing, Supervision, Project administration, Methodology, Funding acquisition, Conceptualization.

Declaration of competing interest

The authors declare that they have no known competing financial interests or personal relationships that could have appeared to influence the work reported in this paper.

Data availability

Data will be made available on request.

Acknowledgments

Fuda Ning would like to acknowledge the support from the U.S. National Science Foundation through award (CMMI-2224309) as well as the grant (#ADLG241) from Small Scale Systems Integration and Packaging (S^3IP) Center of Excellence, funded by New York Empire State Development's Division of Science, Technology and Innovation. Fuji Wang appreciates the support from Liaoning Revitalization Talents Program (Grant No. XLYC1801008, XLYCYSZX1901, and XLYC1902014), Science and Technology Innovation Foundation of Dalian (Grant No. 2019CT01).

Appendix A:. Derivation for Eq. (6)

For the pressure-less anisotropic sintering of the printed 'green' parts, different deformation behaviors along *X* (In-plane), *Y* (In-plane), and *Z* (building) direction should be examined. Specifically, the stress and strain rate tensors can be approximated as:

$$\dot{e}_{ij} = \begin{pmatrix} \dot{e}_x & 0 & 0 \\ 0 & \dot{e}_y & 0 \\ 0 & 0 & \dot{e}_z \end{pmatrix} Anisotropic \dot{e} = \dot{e}_x + \dot{e}_y + \dot{e}_z \tag{19}$$

Combining Eq. (1), we obtain the following modified expression:

$$\sigma_{ij} = 2\eta\left(\varphi\dot{e}_{ij} + \psi\left(\dot{e}_x + \dot{e}_y + \dot{e}_z\right) - \frac{\varphi}{3}\left(\dot{e}_x + \dot{e}_y + \dot{e}_z\right)\right) + P_L\delta_{ij} \tag{20}$$

For pressure-less free sintering in ME process, σ_{ij} is set to 0. And anisotropic shrinkage is first reflected in $\dot{e}_{ij}$. Eq. (20) can be expressed by:

$$0 = 2\eta_x\left(\psi\left(\dot{e}_x + \dot{e}_y + \dot{e}_z\right) + \frac{2\varphi}{3}\dot{e}_x - \frac{\varphi}{3}\left(\dot{e}_y + \dot{e}_z\right)\right) + P_L(\mathrm{X-axis}) \tag{21-1}$$

$$0 = 2\eta_y\left(\psi\left(\dot{e}_x + \dot{e}_y + \dot{e}_z\right) + \frac{2\varphi}{3}\dot{e}_y - \frac{\varphi}{3}\left(\dot{e}_x + \dot{e}_z\right)\right) + P_L(\mathrm{Y-axis}) \tag{21-2}$$

$$0 = 2\eta_z\left(\psi\left(\dot{e}_x + \dot{e}_y + \dot{e}_z\right) + \frac{2\varphi}{3}\dot{e}_z - \frac{\varphi}{3}\left(\dot{e}_x + \dot{e}_y\right)\right) + P_L(\mathrm{Z-axis}) \tag{21-3}$$

Subsequently, the strain rate components in three directions (X, Y, and Z-axis) are isolated separately:

$$\dot{e}_x = \frac{-P_L\left(6\eta_y\eta_z\psi - 3\eta_x\eta_z\psi - 3\eta_x\eta_y\psi + \varphi\eta_x\eta_y + \varphi\eta_x\eta_z + \varphi\eta_y\eta_z\right)}{18\varphi\psi\eta_x\eta_y\eta_z} \tag{22-1}$$

$$\dot{e}_y = \frac{-P_L\left(6\eta_x\eta_z\psi - 3\eta_x\eta_y\psi - 3\eta_y\eta_z\psi + \varphi\eta_x\eta_y + \varphi\eta_x\eta_z + \varphi\eta_y\eta_z\right)}{18\varphi\psi\eta_x\eta_y\eta_z} \tag{22-2}$$

$$\dot{e}_z = \frac{-P_L\left(6\eta_x\eta_y\psi - 3\eta_x\eta_z\psi - 3\eta_y\eta_z\psi + \varphi\eta_x\eta_y + \varphi\eta_x\eta_z + \varphi\eta_y\eta_z\right)}{18\varphi\psi\eta_x\eta_y\eta_z} \tag{22-3}$$

Combining Eq. (22) with Eq. (2), we obtain Eq. (6).

References

[1] C. Groden, K.D. Traxel, E. Ali Afrouzian, A.B. Nyberg, Inconel 718–W7Ni3Fe bimetallic structures using directed energy deposition-based additive manufacturing, Virtual Phys. Prototyp. 17 (2022) 170–180, https://doi.org/10.1080/17452759.2022.2025673.

[2] F. Veron, F. Lanoue, V. Baco-Carles, K. Kiryukhina, O. Vendier, P. Tailhades, Selective laser powder bed fusion for manufacturing of 3D metal-ceramic multi-materials assemblies, Addit. Manuf. 50 (2022) 102550, https://doi.org/10.1016/j.addma.2021.102550.

[3] I. Yadroitsev, I. Yadroitsava, Evaluation of residual stress in stainless steel 316L and Ti6Al4V samples produced by selective laser melting, Virtual Phys. Prototyp. 10 (2015) 67–76, https://doi.org/10.1080/17452759.2015.1026045.

[4] G. Singh, J. Missiaen, D. Bouvard, J. Chaix, Additive manufacturing of 17–4 PH steel using metal injection molding feedstock: Analysis of 3D extrusion printing, debinding and sintering, Addit. Manuf. 47 (2021) 102287, https://doi.org/10.1016/j.addma.2021.102287.

[5] M. Sadaf, M. Bragaglia, F. Nanni, A simple route for additive manufacturing of 316L stainless steel via Fused Filament Fabrication, J. Manuf. Process. 67 (2021) 141–150, https://doi.org/10.1016/j.jmapro.2021.04.055.

[6] B. Liu, Y. Wang, Z. Lin, T. Zhang, Creating metal parts by Fused Deposition Modeling and Sintering, Mater. Lett. 263 (2020) 127252, https://doi.org/10.1016/j.matlet.2019.127252.

[7] M. Galati, P. Minetola, Analysis of density, roughness, and accuracy of the atomic diffusion additive manufacturing (ADAM) process for metal parts, Materials 12 (2019) 1422, https://doi.org/10.3390/ma12244122.

[8] Y. Zhang, S. Bai, M. Riede, E. Garratt, A. Roch, A comprehensive study on fused filament fabrication of Ti-6Al-4V structures, Addit. Manuf. 34 (2020) 101256, https://doi.org/10.1016/j.addma.2020.101256.

[9] G. Singh, J. Missiaen, D. Bouvard, J. Chaix, Copper extrusion 3D printing using metal injection moulding feedstock: Analysis of process parameters for green density and surface roughness optimization, Addit. Manuf. 38 (2021) 101778, https://doi.org/10.1016/j.addma.2020.101778.

[10] M. Mohammadizadeh, H. Lu, I. Fidan, K. Tantawi, A. Gupta, S. Hasanov, Z. Zhang, F. Alifui-Segbaya, A. Rennie, Mechanical and thermal analyses of metal-pla components fabricated by metal material extrusion, Inventions 5 (2020) 44, https://doi.org/10.3390/inventions5030044.

[11] Z. Zhang, I. Fidan, Machine learning-based void percentage analysis of components fabricated with the low-cost metal material extrusion process, Materials 15 (2022) 12, https://doi.org/10.3390/ma15124292.

[12] A. Bose, C.A. Schuh, J.C. Tobia, N. Tuncer, N.M. Mykulowycz, A. Preston, A. C. Barbati, B. Kernan, M.A. Gibson, D. Krause, T. Brzezinski, J. Schroers, R. Fulop, J.S. Myerberg, M. Sowerbutts, Y. Chiang, A. John Hart, E.M. Sachs, A.C. Lund, Traditional and additive manufacturing of a new Tungsten heavy alloy alternative, Int. J. Refract. Hard Met. 73 (2018) 22–28, https://doi.org/10.1016/j.ijrmhm.2018.01.019.

[13] K. Rane, M.A. Farid, W. Hassan, M. Strano, Effect of printing parameters on mechanical properties of extrusion-based additively manufactured ceramic parts,

Ceram. Int. 47 (2021) 12189–12198, https://doi.org/10.1016/j.ceramint.2021.01.066.
[14] M. Orlovská, M. Hain, M. Kitzmantel, P. Veteška, Z. Hajdúchová, M. Janek, M. Vozárová, Ľ. Bača, Monitoring of critical processing steps during the production of high dense 3D alumina parts using Fused Filament Fabrication technology, Addit. Manuf. 48 (2021) 102395, https://doi.org/10.1016/j.addma.2021.102395.
[15] J.D. Powers, A.M. Glaeser, Grain boundary migration in ceramics, Interface Sci. 6 (1998) 23–39, https://doi.org/10.1023/A:1008656302007.
[16] Y. Thompson, J. Gonzalez-Gutierrez, C. Kukla, P. Felfer, Fused filament fabrication, debinding and sintering as a low cost additive manufacturing method of 316L stainless steel, Addit. Manuf. 30 (2019) 100861, https://doi.org/10.1016/j.addma.2019.100861.
[17] D. Jiang, F. Ning, Additive manufacturing of 316L stainless steel by a printing-debinding-sintering method: effects of microstructure on fatigue property, J. Manuf. Sci. E-T. ASME. 143 (2021) 091007, https://doi.org/10.1115/1.4050190.
[18] R. Santamaria, M. Salasi, S. Bakhtiari, G. Leadbeater, M. Iannuzzi, M.Z. Quadir, Microstructure and mechanical behaviour of 316L stainless steel produced using sinter-based extrusion additive manufacturing, J. Mater. Sci. 57 (2022) 9646–9662, https://doi.org/10.1007/s10853-021-06828-8.
[19] J. Damon, S. Dietrich, S. Gorantla, U. Popp, B. Okolo, V. Schulze, Process porosity and mechanical performance of fused filament fabricated 316L stainless steel, Rapid Prototyp. J. 25 (2019) 1319–1327, https://doi.org/10.1108/RPJ-01-2019-0002.
[20] H. Gong, C. Crater, A. Ordonez, C. Ward, M. Waller, C. Ginn, Material properties and shrinkage of 3D printing parts using ultrafuse stainless steel 316LX filament, ICMMM 2018 (249) (2018) 01001, https://doi.org/10.1051/matecconf/201824901001.
[21] Y. Wang, L. Zhang, X. Li, Z. Yan, On hot isostatic pressing sintering of fused filament fabricated 316L stainless steel-evaluation of microstructure, porosity, and tensile properties, Mater. Lett. 296 (2021) 129854, https://doi.org/10.1016/j.matlet.2021.129854.
[22] M.N. Rahaman, Sintering of ceramics, CRC Press, 2007.
[23] R.K. Bordia, S.J.L. Kang, E.A. Olevsky, Current understanding and future research directions at the onset of the next century of sintering science and technology, J. Am. Ceram. Soc. 100 (2017) 2314–2352, https://doi.org/10.1111/jace.14919.
[24] S.L. Kang, Y. Jung, Sintering kinetics at final stage sintering: model calculation and map construction, Acta Mater. 52 (2004) 4573–4578, https://doi.org/10.1016/j.actamat.2004.06.015.
[25] H. Riedel, J. Svoboda, A theoretical study of grain growth in porous solids during sintering, Acta Metall. 41 (1993) 1929–1936, https://doi.org/10.1016/0956-7151(93)90212-B.
[26] R. Watanabe, Y. Masuda, Quantitative estimation of structural change in carbonyl iron powder compacts during sintering, Trans. Japan Inst. Met. 13 (1972) 134, https://doi.org/10.2320/matertrans1960.13.134.
[27] G. Kerbart, C. Manière, C. Harnois, S. Marinel, Predicting final stage sintering grain growth affected by porosity, Appl. Mater. Today 20 (2020) 100759, https://doi.org/10.1016/j.apmt.2020.100759.
[28] C. Manière, S. Chan, G. Lee, J. McKittrick, E.A. Olevsky, Sintering dilatometry based grain growth assessment, Results Phys. 10 (2018) 91–93, https://doi.org/10.1016/j.rinp.2018.05.014.
[29] C. Manière, G. Leea, J. McKittrick, S. Chan, E.A. Olevsky, Modeling zirconia sintering trajectory for obtaining translucent submicronic ceramics for dental implant applications, Acta Mater. 188 (2020) 101–107, https://doi.org/10.1016/j.actamat.2020.01.061.
[30] E.A. Olevsky, C. Garcia-Cardona, W.L. Bradbury, C.D. Haines, D.G. Martin, D. Kapoor, Fundamental aspects of spark plasma sintering: ii. finite element analysis of scalability, J. Am. Ceram. Soc. 95 (2012) 2414–2422, https://doi.org/10.1111/j.1551-2916.2012.05096.x.
[31] E.A. Olevsky, Theory of sintering: from discrete to continuum, Mater. Sci. Eng. R. Rep. 23 (1998) 41–100, https://doi.org/10.1016/S0927-796X(98)00009-6.
[32] J. Zhao, M.P. Harmer, Effect of pore distribution on microstructure development: i, matrix pores, J. Am. Ceram. Soc. 71 (1988) 113–120, https://doi.org/10.1111/j.1151-2916.1988.tb05826.x.
[33] J. Zhao, M.P. Harmer, Effect of pore distribution on microstructure development: ii, first- and second-generation pores, J. Am. Ceram. Soc. 71 (1988) 530–539, https://doi.org/10.1111/j.1151-2916.1988.tb05916.x.
[34] J. Zhao, M.P. Harmer, Effect of pore distribution on microstructure development: iii, model experiments, J. Am. Ceram. Soc. 75 (1992) 830–843, https://doi.org/10.1111/j.1151-2916.1992.tb04148.x.
[35] S. You, D. Jiang, F. Wang, F. Ning, Anisotropic sintering shrinkage behavior of stainless steel fabricated by extrusion-based metal additive manufacturing, J. Manuf. Process. 101 (2023) 1508–1520, https://doi.org/10.1016/j.jmapro.2023.07.026.
[36] Ultrafuse 316L User Guidelines for 3D Printing Metal Parts. https://forward-am.com/wp-content/uploads/2020/05/User-Guidelines.pdf.
[37] D. Huber, L. Vogel, A. Fischer, The effects of sintering temperature and hold time on densification, mechanical properties and microstructural characteristics of binder jet 3D printed 17–4 PH stainless steel, Addit. Manuf. 46 (2021) 102114, https://doi.org/10.1016/j.addma.2021.102114.
[38] D. Jiang, F. Ning, Anisotropic deformation of 316L stainless steel overhang structures built by material extrusion based additive manufacturing, Addit. Manuf. 50 (2022) 102545, https://doi.org/10.1016/j.addma.2021.102545.
[39] P. Suri, R.P. Koseski, R.M. German, Microstructural evolution of injection molded gas- and water-atomized 316L stainless steel powder during sintering, Mater. Sci. Eng. A 402 (2005) 341–348, https://doi.org/10.1016/j.msea.2005.01.004.6.
[40] C. Manière, E. Saccardo, G. Leea, J. McKittrick, A. Molinari, E.A. Olevsky, Swelling negation during sintering of sterling silver: An experimental and theoretical approach, Results Phys. 11 (2018) 79–84, https://doi.org/10.1016/j.rinp.2018.08.035.
[41] C. Manière, G. Kerbart, C. Harnois, S. Marinel, Modeling sintering anisotropy in ceramic stereolithography of silica, Acta Mater. 182 (2020) 163–171, https://doi.org/10.1016/j.actamat.2019.10.032.
[42] Z. Li, T. Voisin, J.T. Mckeown, J. Ye, T. Braun, C. Kamath, W.E. King, Y.M. Wang, Tensile properties, strain rate sensitivity, and activation volume of additively manufactured 316L stainless steels, Int. J. Plast 120 (2019) 395–410, https://doi.org/10.1016/j.ijplas.2019.05.009.
[43] R. Zhang, R.S. Engel, N.J. Salamon, R.M. German, Finite element analysis on the sintering of stainless steel 316L powder compacts, Adv. Powder Metall. Part. Mater. 9 (2002) 9–60.
[44] R.J. Brook, Pore-grain boundary interactions and grain growth, J. Am. Ceram. Soc. 52 (1969) 56, https://doi.org/10.1111/j.1151-2916.1969.tb12664.x.
[45] K.D. Zilnyk, G.S. Leite, H.R.Z. Sandim, P.R. Rios, Grain growth inhibition by connected porosity in sintered niobium, Acta Mater. 61 (2013) 5821–5828, https://doi.org/10.1016/j.actamat.2013.06.027.
[46] P.R. Rios, G. Gottstein, L.S. Shvindlerman, An irreversible thermodynamic approach to normal grain growth with a pinning force, Mater. Sci. Eng. A 332 (2002) 231–235, https://doi.org/10.1016/S0921-5093(01)01745-2.
[47] S.J. Park, P. Suri, E.A. Olevsky, R.M. German, Master sintering curve formulated from constitutive models, J. Am. Ceram. Soc. 92 (2009) 1410–1413, https://doi.org/10.1111/j.1551-2916.2009.02983.x.
[48] Y. Mishin, Solute drag and dynamic phase transformations in moving grain boundaries, Acta Mater. 179 (2019) 383–395, https://doi.org/10.1016/j.actamat.2019.08.046.
[49] J.W. Cahn, The impurity-drag effect in grain boundary motion, Acta Metall. 10 (1962) 789, https://doi.org/10.1016/0001-6160(62)90092-5.
[50] F. Wang, S. You, D. Jiang, F. Ning, Study on sintering mechanism for extrusion-based additive manufacturing of stainless steel through molecular dynamics simulation, Addit. Manuf. 58 (2022) 102991, https://doi.org/10.1016/j.addma.2022.102991.
[51] J. Poetschke, V. Richter, R. Holke, Influence and effectivity of VC and Cr_3C_2 grain growth inhibitors on sintering of binderless tungsten carbide, Int J Refract Hard Met. 31 (2012) 218–223, https://doi.org/10.1016/j.ijrmhm.2011.11.006.